CrossMark

Substrate-Independent Lattice Plasmon Modes for High-Performance On-Chip Plasmonic Sensors

Linhan Lin[1] · Yuebing Zheng[1]

Abstract We systematically study the lattice plasmon resonance structures, which are known as core/shell SiO$_2$/Au nanocylinder arrays (NCAs), for high-performance, on-chip plasmonic sensors using the substrate-independent lattice plasmon modes (LPMs). Our finite-difference time-domain simulations reveal that new modes of localized surface plasmon resonances (LSPRs) show up when the height-diameter aspect ratio of the NCAs is increased. The height-induced LSPRs couple with the superstrate diffraction orders to generate the substrate-independent LPMs. Moreover, we show that the high wavelength sensitivity and the narrow linewidth of the substrate-independent LPMs lead to the plasmonic sensors with high figure of merit (FOM) and high signal-to-noise ratio (SNR). In addition, the plasmonic sensors are robust in asymmetric environments for a wide range of working wavelengths. Our further study of both far- and near-field electromagnetic distribution in the NCAs confirms the height-enabled tunability of the plasmonic "hot spots" at the sub-nanoparticle resolution and the large field enhancement in the substrate-independent LPMs, which are responsible for the high FOM and SNR of the plasmonic sensors.

✉ Yuebing Zheng
zheng@austin.utexas.edu

[1] Department of Mechanical Engineering, Materials Science & Engineering Program, and Texas Materials Institute, The University of Texas at Austin, Austin, TX 78712, USA

Introduction

Noble metal nanoparticles (NPs) such as Au NPs and Ag NPs support localized surface plasmon resonances (LSPRs), which are the light-coupled coherent oscillations of free electrons confined within the NPs [1–5]. Various applications such as enhanced spontaneous or stimulated emission [6–8], solar energy harvesting [9–14], surface-enhanced Raman spectroscopy, [15–18] and cancer phototherapy [19, 20] have been investigated. Due to the strong electromagnetic field confinement and enhancement at the nanoscale, LSPRs are highly sensitive to the refractive index (RI) of local environments of the NPs, enabling the development of plasmonic sensors based on the analyte-induced changes in the peak wavelength and/or intensity of LSPRs [21–26].

According to Drude model, the real part of dielectric function of metal is expressed as [27]

$$\varepsilon_1 = 1 - \frac{\omega_p{}^2}{\omega^2 + \gamma^2}, \tag{1}$$

where ω_p is the plasma frequency and γ is the damping parameter of bulk metal. γ is negligible in visible and infrared wavelength. At resonance wavelength, $\varepsilon_1 = -2\varepsilon_m = -2n_m{}^2$, where ε_m and n_m are dielectric function and RI of the media surrounding the metal NPs, respectively. Therefore, the peak wavelength of LSPRs is expressed as

$$\lambda_m = \lambda_p \sqrt{2n_m{}^2 + 1}, \tag{2}$$

where λ_p is the wavelength calculated according to the plasma frequency as $2\pi c/\omega_p$. The nearly linear relationship between the resonance wavelength and RI in surrounding media underpins the plasmonic sensors employing LSPRs. The wavelength sensitivity of the plasmonic sensors that operate under

wavelength-shift mode reaches hundreds of nanometers per RI unit (RIU) [28–30].

The performances of plasmonic sensors can be characterized by their figure of merit (FOM), which is defined as ratio of the wavelength sensitivity and the resonance linewidth. Usually, Ag nanospheres [30] and Au nanospheres [31] as single NPs or uncoupled arrays [32–34] have FOM between 1 and 3. The FOM is limited by the broad linewidth of LSPRs caused by radiative damping [35–38]. Immobilizing NPs on substrates as required for on-chip applications also reduces FOM due to the reduced sensing areas from the contact between the NPs and the substrates. Strategies have been developed to improve the FOM of on-chip plasmonic sensors. For example, substrate undercutting has been applied to reduce the NP-substrate contact areas in order to increase the wavelength sensitivity [39]. The design of NPs with sharp tips, like Ag nanotriangles [30] or Au nanostars, [40] has enhanced the FOM up to 5. A significant improvement of FOM has been achieved by breaking the symmetry in two or more NPs (or nanoholes) to introduce the Fano resonances with narrow linewidth, [41, 42] which result from interaction between a discrete state and a continuum of states [43].

Another effective approach towards narrowing the resonance linewidth of LSPRs is to arrange NPs in a highly ordered array so that far-field diffractive coupling occurs [44, 45]. When the diffraction orders change from evanescent to radiative, a strong dipolar interaction occurs, resulting in lattice plasmon modes (LPMs) or collective modes [46–57]. Significant suppression of the radiative damping leads to an ultra-narrow resonance linewidth of LPMs. Both theoretical and experimental studies have shown that the narrow linewidth leads to the enhanced performance in sensing [58–61]. However, the LPMs have intrinsic drawback for sensing applications due to their requirement of homogeneous environments surrounding the arrays of NPs. The LPMs are suppressed when the NPs are immobilized on substrates because the diffraction orders are cut off at the nanoparticle-substrate interfaces [62]. One can avoid this drawback by either introducing an index-matching layer on the top of NPs to generate a quasi-symmetric environment or increasing the size of the NPs to obtain coupling at the higher polarizability [51, 60, 62]. However, the index-matching layer prevents the interactions between analytes and NPs, and the use of larger NPs reduces the range of working wavelengths, limiting the applications of LPMs in the on-chip sensors [59, 60, 63]. Recently, an extremely high FOM of 108 is reported for LPMs in the Au mushroom arrays [64]. However, the weak coupling in this type of structures leads to a low signal-to-noise ratio (SNR). As a result, the development of LPM-based plasmonic sensors with both high FOM and SNR for a wide range of working wavelengths in the asymmetric environment has remained challenging.

Herein, we introduce an approach towards increasing the FOM of on-chip plasmonic sensors for a wide range of working wavelengths, which synergizes the sub-nanoparticle engineering of plasmonic "hot spots" for high sensitivity and narrow linewidth of the LPMs. Previous work has demonstrated that the height-induced LPMs in the core/shell SiO_2/Au nanocylinder arrays (NCAs) [65, 66] shift the plasmonic "hot spots" from the nanoparticle-substrate interface to the nanoparticle-superstrate interface to form the substrate-independent modes. In this study, we focus on evaluating the sensing capability of the substrate-independent LPMs. Our studies are based on finite-difference time-domain (FDTD) simulations, and the far-field sensing performances are supported by the studies of near-field electromagnetic field distribution.

Simulation Details

Figure 1 illustrates the design of our plasmonic sensor, which consists of the core/shell SiO_2/Au NCAs on a SiO_2 substrate, and the experimental setup for evaluating the sensing performances. The diameter (D) of the SiO_2 nanocylinders (NCs) ranges from 50 to 250 nm, while the height (h) is changed from 50 to 400 nm. Since the resonance wavelength of the LSPRs of the core/shell NCs depends on the ratio of the total diameter to the core diameter, we fix the thickness of the outer Au layer at 20 nm to simplify the simulations [67]. The lattice constants are defined with reference to the polarization of the incident light, i.e., $a_\parallel$ when the direction is parallel to the electric field (E_x) of incident light and $a_\perp$ when the direction is vertical to the electric field. The optical constants of Au were taken from Johnson and Christy [68].

Results and Discussions

Hot Spots Engineering in Single NC

As a reference to the design of the proposed plasmonic sensors based on the NCAs, we first examine the LSPR modes and FOM of single core/shell SiO_2/Au NCs with different height-diameter aspect ratios on SiO_2 substrates. As shown in Fig. 2a, the single NC with a low aspect ratio ($D = 200$ nm and $h = 50$ nm) exhibits a dipole-bonding mode (D_1 mode) at a peak wavelength of 1049 nm when the superstrate RI is 1.0. The peak wavelength of the D_1 mode makes a continuous redshift when the superstrate RI is increased from 1.0 to 1.2. Due to the radiative damping in the LSPRs, the linewidth of the scattering spectra is broad. The full width at half maximum (FWHM) for the spectrum with RI = 1.0 is 287 nm. The FWHM increases with RI and reaches 372 nm when RI = 1.2. It has been shown that an increased radiation damping and FWHM can be caused by the increased NP volume [35, 36, 69]. Although the actual volume of the NC
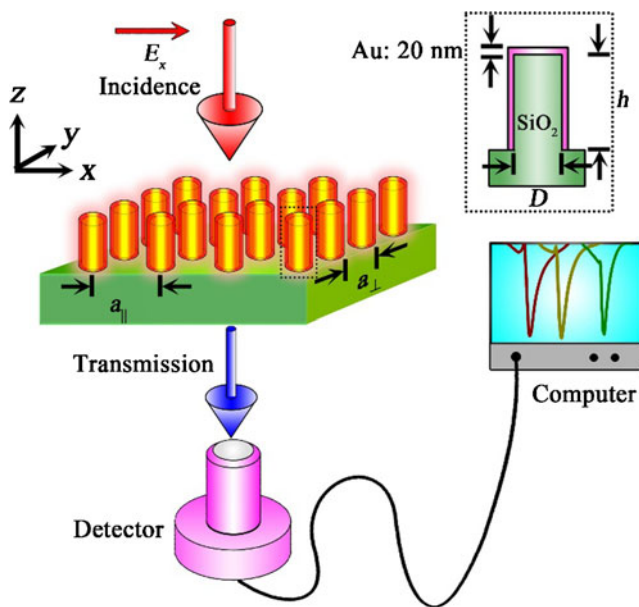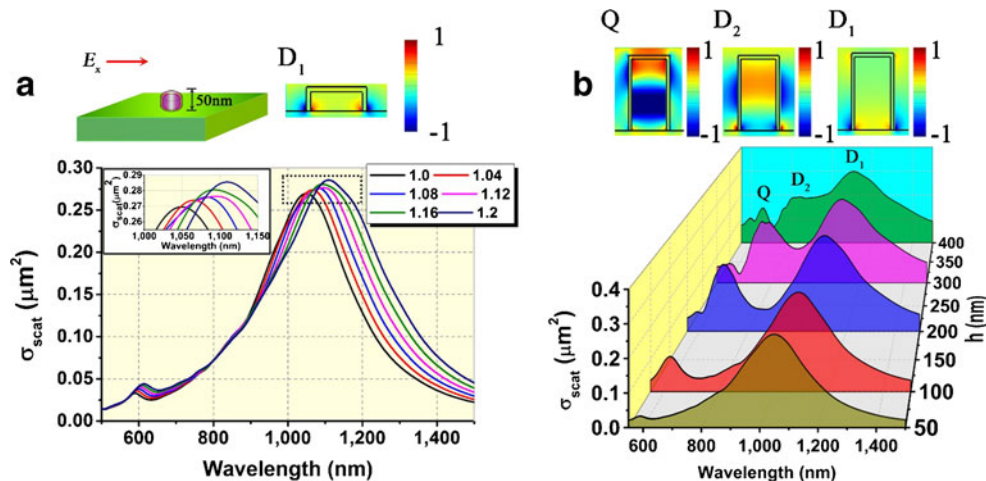
Fig. 1 Schematic of the plasmonic sensor consisting of the core/shell SiO₂/Au NCAs on a SiO₂ substrate and the experimental setup for the performance characterization. Incident light (*red arrow*) is launched normal onto the sample, and transmission light (*blue arrow*) is collected. A shift of the resonance wavelength in the transmission spectra is monitored to measure the changes of RI in the superstrate

We hypothesize that one can enhance the wavelength sensitivity of the LSPRs of single NCs to the superstrate RI (i.e., analytes) by shifting the plasmonic "hot spots" away from the nanoparticle-substrate interface to maximize their interactions with analytes. To test this hypothesis, we achieve the spatial control of the plasmonic "hot spots" within NCs at the sub-nanoparticle resolution by tuning the height-diameter aspect ratio of the NCs. Figure 2b shows the simulated scattering spectra and the near-field electromagnetic fields of single NCs with different heights for superstrate RI = 1.0. We observe a strong dependence of the LSPRs on the height of the NCs. Firstly, the D_1 mode makes a slight redshift with the increased height. Secondly, a new dipole-bonding mode (D_2 mode) shows up at the shorter wavelength of the D_1 mode. With the "hot spots" located at the side of the NC (see upper panel of Fig. 2b), the D_2 mode makes a redshift with the increased height. Lastly, a quadrupole mode (Q mode) appears at the higher energy side of the D_2 mode when the height of the NC is further increased (i.e., $h > 300$ nm). This higher-order mode has the "hot spots" both within the core at the bottom of the NC and at the outer part of the Au shell on the top of the NC. Compared with the FOM of D_1 mode (<0.98) in Fig. 2a, the D_2 mode and Q mode have larger FOM, which are 3.15 ($h = 200$ nm; RI = 1) and 5.95 ($h = 400$ nm; RI = 1) (not shown here). The higher FOM for the D_2 and Q modes justifies our hypothesis that the shift of the "hot spots" away from the nanoparticle-substrate interface increases the FOM. We focus on the height-induced D_2 mode because it provides the opportunity to couple with the superstrate diffraction orders to generate the substrate-independent LPMs in 2D NCAs, which enables the development of the high-FOM plasmonic sensors.

remains the same for the different RIs (Fig. 2a), the NC experiences an increased volume because of a decreased effective wavelength of incident light when the surrounding medium has higher RI. Our further study of the near-field electromagnetic (E_x component) distribution at the NC (see upper panel of Fig. 2a) reveals that the LSPR of single NC originates from the propagation interruption at the interface between the NC and the substrate. Since the plasmonic "hot spots" associated with D_1 mode interface with both substrate and superstrate, the sensitivity of the LSPR to the superstrate RI is low. From Fig. 2a, we obtain a wavelength sensitivity of 280 nm/RIU and a FOM of <0.98.

Enhanced FOM in the Core/Shell NCAs

To study the height-induced LPMs in the 2D NCAs, we choose the NCs with the diameter $D = 200$ nm and the height $h = 400$ nm, which exhibit strong D_2 mode. When light is

Fig. 2 Simulated scattering spectra of single core/shell SiO₂/Au NC on SiO₂ substrate with $D = 200$ nm. **a** $h = 50$ nm, superstrate RI changes from 1.0 to 1.2, and the real part of E_x is illustrated for RI = 1.0. The *inset* shows the enlarged scattering spectra in the spectral range indicated by the dash box. **b** RI = 1.0, the height of NC (i.e., h) changes from 50 to 400 nm, and the real part of E_x is illustrated for Q mode, D_2 mode, and D_1 mode for NC with $h = 400$ nm

incident on the 2D NCAs, photonic diffraction orders occur under specific conditions. The diffraction orders are calculated by treating the out-of-plane wave number as zero, which is given by

$$k_{i,j}^{\perp} = \sqrt{\left(n\frac{2\pi}{\lambda}\right)^2 - k_{i,j}^{\parallel}{}^2} = 2\pi\sqrt{\frac{n^2}{\lambda^2} - \frac{i^2}{a_x{}^2} - \frac{j^2}{a_y{}^2}}, \qquad (3)$$

where n is the RI of the media surrounding the NCAs, λ is the wavelength of the incident light, and $k_{i,j}^{\parallel}$ is the in-plane wave number, which is determined by the lattice constants of the NCAs a_x and a_y (corresponding to $a_\parallel$ and $a_\perp$ in Fig. 1). The different diffraction orders along the x and y axes are determined by the integers i and j, respectively. When orthogonal coupling (i.e., the electric field E_x of incident light is vertical to $a_\perp$ as shown in Fig. 1) is considered, the wavelength of the $(0, j)$ diffraction orders is simplified as

$$\lambda_{0,j} = na\perp/|j|, \qquad (4)$$

Therefore, the coupling can be controlled by tuning the lattice constants of the NCAs. When the lattice constants of the NCAs are set as 500 nm for both x and y directions, the diffraction orders have no overlap with the LSPRs of the NCs and no photonic-plasmonic coupling occurs. Figure 3a shows a series of transmission spectra of the NCAs ($D = 200$ nm and $h = 400$ nm) when the superstrate RI changes from 1.0 to 1.2. Without the coupling, the transmission spectra of the NCAs are similar to that of the single NC with the same diameter, height, and RI (Fig. 2b). It should be noted that the transmission spectra, which arise from both light absorption and backward scattering by the NCAs, are different from the scattering spectra in Fig. 2b. However, both types of spectra can reveal the characteristics of the various modes of the LSPRs. As shown in Fig. 3a, the D_1 mode shows up in the transmission spectra of the NCAs as dips around the wavelength of 1000 nm. Similarly, the D_1 mode has a relatively low sensitivity to the changes of the superstrate RI (133 nm/RIU). The dips at 660 and 750 nm (referring to the spectrum for RI = 1 in Fig. 3a) correspond to the Q mode and D_2 mode (also see Fig. 2b), respectively [65]. The wavelength sensitivity of the Q mode is calculated as 411 nm/RIU, which is higher than that of D_1 mode. Like single NC, the enhanced wavelength sensitivity of the Q mode is attributed to the "hot spots" located at the sides of the NCs. The FWHM of the Q mode is calculated as 50 nm for RI = 1, leading to a high FOM of 8.2. The D_2 mode merges with other modes at the higher superstrate RI, which makes it challenging to quantify the corresponding FOM.

To enable the plasmonic-photonic coupling for the LPMs in the NCAs, we tune the lattice constants to make the diffraction orders overlap with the LSPRs, in particular, the D_2 mode. We focus on the D_2 mode because its plasmonic "hot spots" located at the sides of the NCs can couple with the superstrate

diffraction waves to generate the substrate-independent LPMs for the enhanced sensing performance. Figure 3b shows a series of transmission spectra of the NCAs ($D = 200$ nm, $h = 400$ nm, and $a_\perp = 900$ nm), which exhibit the coupling and the LPMs, when the superstrate RI changes from 1.0 to 1.2. A strong dip at the wavelength of 937 nm in the spectrum (for RI = 1) is assigned to the LPM that arises from the coupling between the $(0, \pm1)$ superstrate diffraction orders and the D_2 mode. This LPM makes a continuous redshift when the RI is increased, leading to a sensitivity of 733 nm/RIU. The increased sensitivity of the LPM is attributed to the high sensitivity of the superstrate diffraction orders to the changes of superstrate RI. As radiative damping is suppressed in this collective mode, the LPM has a linewidth that is much smaller than that of the LSPRs of single NCs. Even if we take an intermediate FWHM value from the spectrum with RI = 1.08, a high FOM of 17.9 is obtained. In contrast, the LPM that arises from the coupling between the $(0, \pm1)$ substrate diffraction orders and the D_1 mode is not sensitive to the superstrate RI. Such a LPM is identified as a dip around the wavelength of 1258 nm in the spectra of Fig. 3b. When the superstrate RI changes from 1.0 to 1.2, the dip wavelength of this substrate-related LPM has almost remained unchanged.

To better understand the two types of LPMs in Fig. 3b, we describe the $(0, \pm1)$ diffraction orders as $\lambda_{0,j} = na_\perp/|j|$ according to Eq. 4. We can see that the resonance wavelength is proportional to the RI of media surrounding the NCAs (i.e., n in Eq. 4) and to the lattice constants that are perpendicular to the external electric field E_x of incident light. Since n can be the RI of either superstrate or substrate, two sets of diffraction orders exist. For the LPM that arises from the coupling between the D_2 mode and the $(0, \pm1)$ superstrate diffraction orders, the increase of superstrate RI makes a redshift in both the superstrate diffraction orders and the D_2 mode, leading to the redshift of the LPM accordingly. The Fano-like LPM can be explained by the coupling between the discrete state (diffraction orders) and a continuum of states (LSPRs), and therefore, the coupling wavelength is slightly deviated from the $(0, \pm1)$ superstrate diffraction orders. This deviation is responsible for the difference in the wavelength sensitivity between the LPM and the $(0, \pm1)$ superstrate diffraction orders, i.e., 733 nm/RIU versus 900 nm/RIU (according to Eq. 4).

Electromagnetic Field Distribution and SNR

To gain a deeper insight into the photonic-plasmonic coupling and the field enhancement, we further study the electromagnetic field distribution in the NCAs. A large field enhancement is highly desired to achieve the plasmonic sensors with large extinction efficiency and thus high SNR. Figure 4 shows the field intensity distribution at an NC within the NCAs ($D = 200$ nm, $a_\parallel = 500$ nm, $h = 400$ nm, and superstrate RI = 1) with different $a_\perp$ and λ. Figure 4a shows the electric
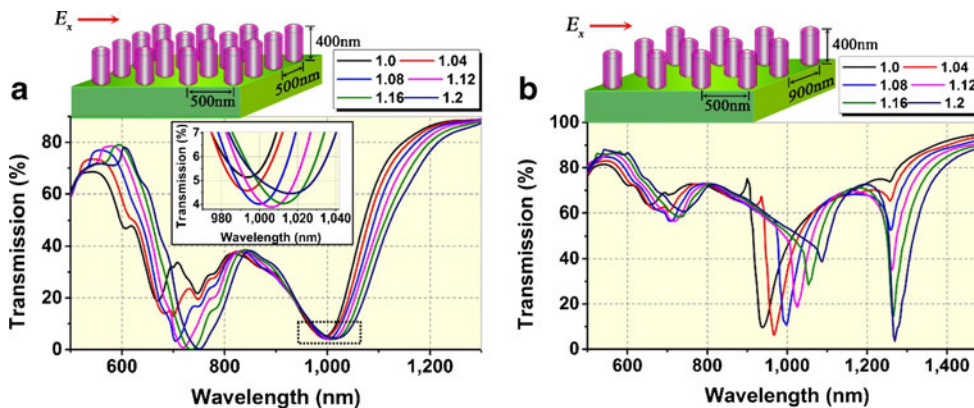
Fig. 3 Simulated transmission spectra of the core/shell SiO$_2$/Au NCAs of two types of $a_\perp$ on the SiO$_2$ substrates as a function of the superstrate RI, which changes from 1.0 to 1.2. The NCAs have $D = 200$ nm, $a_\parallel = 500$ nm, $h = 400$ nm, and **a** $a_\perp = 500$ nm, **b** $a_\perp = 900$ nm. The *inset* of **a** shows the enlarged transmission spectra in the spectral range indicated by the *dash box*

field distribution of the D$_2$ mode without the coupling when $a_\perp = 500$ nm and $\lambda = 750$ nm (see Fig. 3a for the spectrum). We can see that the D$_2$ mode arises from the bonding interaction between the inner and outer dipoles and a weak electric field also exists inside the SiO$_2$ core of the NC. Once the D$_2$ mode couples with the $(0, \pm1)$ superstrate diffraction orders to generate the LPM when $a_\perp = 900$ nm and $\lambda = 937$ nm (see Fig. 3b for the spectrum), the inner electric field disappears and the outer electric field is significantly enhanced (Fig. 4b). Therefore, the LPM arises from the far-field radiative interaction between the D$_2$ mode on the NCs, which is the collective behavior caused by the electric field from both incident light and other NCs in the structures.

To further examine the plasmonic enhancement of the field in the diffraction orders, we simulate the magnetic field distributions for both the bare SiO$_2$ NCs (without Au shells) and the core/shell SiO$_2$/Au NCs. The orthogonal diffraction orders lead to the horizontal propagating magnetic field, i.e., H_z component propagating along y axis (see Fig. 1) [65, 66]. Figure 4c shows that, for the bare SiO$_2$ arrays, the superstrate

diffraction order of a low intensity is extended from the sides of the NC into the superstrate with two lobes parallel to z axis. The similar lobes with weaker intensity exist in the substrate, which arises from the imaginary part of H_z rather than the diffraction orders. When the plasmonic-photonic coupling occurs in the core/shell NCAs, the H_z intensity is enhanced with a factor of 20~30, indicating an energy transfer from the plasmonic mode to the photonic diffraction modes (Fig. 4d).

In order to understand the RI-dependent extinction intensity (i.e., the extinction intensity increases and then decrease when the RI changes from 1.0 to 1.2) of the height-induced LPMs in Fig. 3b, we study both near-field and far-field intensity distributions in the NCAs as a function of the superstrate RI. As shown in Fig. 5, the coupling becomes stronger when RI is increased from 1.0 to 1.04 due to the increased near-field electric intensity (Figs. 4b vs. 5a) and far-field magnetic intensity (Figs. 4d vs. 5c). However, the coupling strength becomes weaker when the RI is further increased. The decrease in both near-field electric intensity and far-field magnetic intensity (Fig. 5b, d

Fig. 4 $|E_x|^2$ in the xz plane and $|H_z|^2$ in the yz plane through the center of an NC in the NCAs (also see Fig. 1). The NCAs have $D = 200$ nm, $a_\parallel = 500$ nm, $h = 400$ nm, and RI = 1. **a** $a_\perp = 500$ nm, $\lambda = 750$ nm, **b** $a_\perp = 900$ nm, $\lambda = 937$ nm, **c** $a_\perp = 900$ nm, $\lambda = 897$ nm (bare SiO$_2$ NCAs), and **d** $a_\perp = 900$ nm, $\lambda = 900$ nm
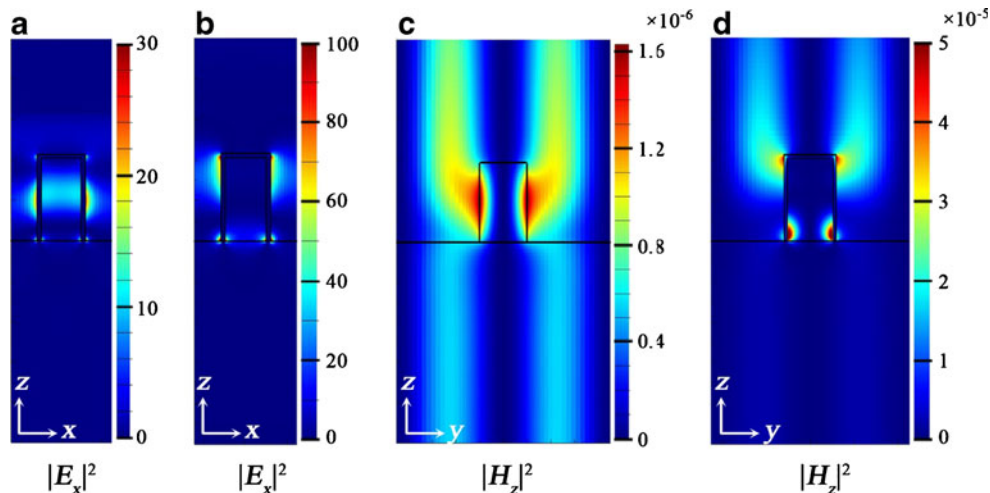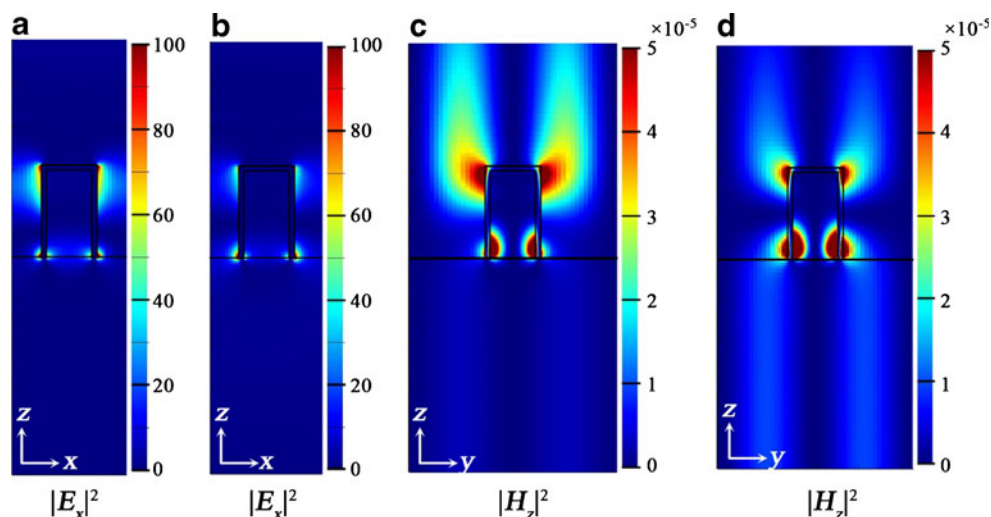
Fig. 5 $|E_x|^2$ in the xz plane and $|H_z|^2$ in the yz plane through the center of an NC in the NCAs (also see Fig. 1). The NCAs have $D = 200$ nm, $a_\parallel = 500$ nm, $a_\perp = 900$ nm, and $h = 400$ nm. **a** RI = 1.04, $\lambda = 967$ nm; **b** RI = 1.2, $\lambda = 1087$ nm; **c** RI = 1.04, $\lambda = 941$ nm; and **d** RI = 1.2, $\lambda = 1087$ nm. The different λ for **a** and **c** is due to the deviation between the discrete state (diffraction orders) and a continuum of states (LSPRs) in the Fano-like coupling of the LPMs

vs. Fig. 5a, c) confirms the decreased coupling strength when RI reaches 1.2. The RI-dependent field intensity matches the dependence of the extinction intensity on the RI (Fig. 3b). This RI dependence indicates the possibility to design the intensity-dependent plasmonic sensors. For the wavelength-dependent sensors, the understanding of the RI dependency helps guide on the design of the parameters of the NCAs to achieve a high extinction ratio (and a high SNR) for target analytes with RI in a specific range.

Fig. 6 Transmission spectra of the core/shell SiO$_2$/Au NCAs on the SiO$_2$ substrates. The height is set as $h = 400$ nm. **a** $D = 50$ nm, $a_\parallel = 300$ nm, $a_\perp = 550$ nm, **b** $D = 100$ nm, $a_\parallel = 400$ nm, $a_\perp = 700$ nm, and **c** $D = 250$ nm, $a_\parallel = 500$ nm, $a_\perp = 1000$ nm. The superstrate RI changes from 1.0 to 1.2. **d** The dependence of the coupling wavelength and the FWHM of the core/shell SiO$_2$/Au NCAs on the diameters of the NCs and the superstrate RI
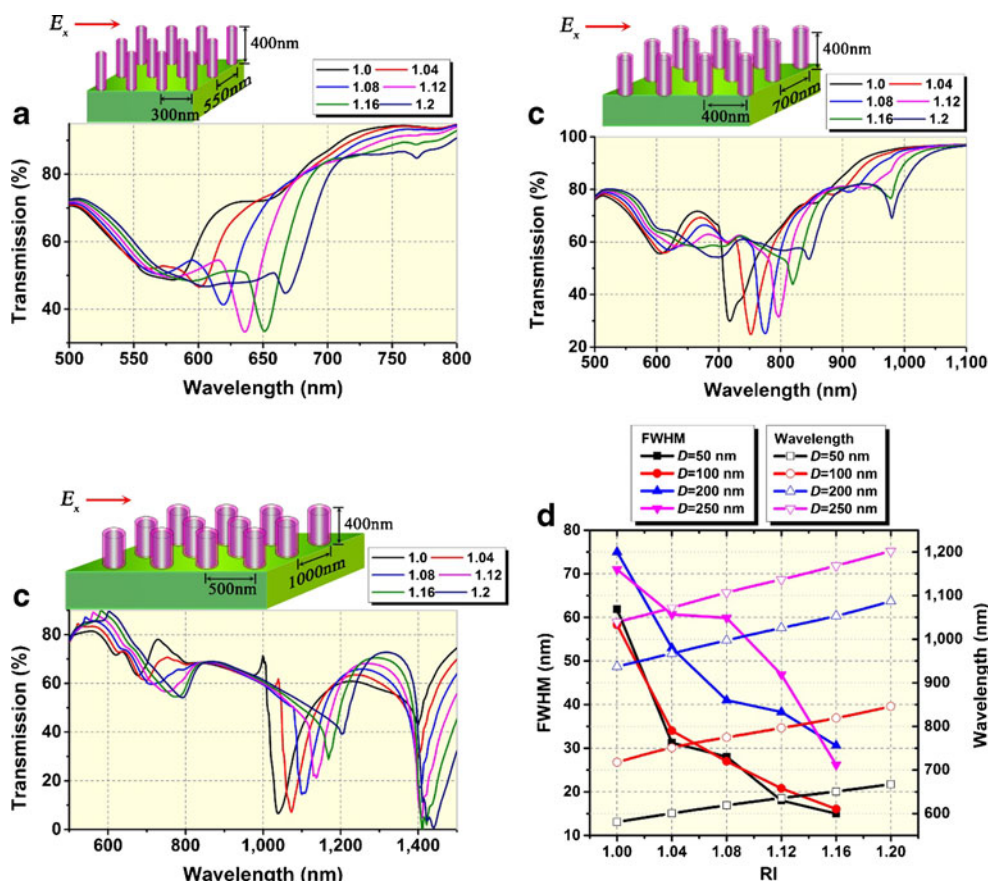
Working Wavelengths of Plasmonic Sensors

To generalize the concept of the height-induced LPMs for the high-performance, on-chip plasmonic sensors, we study the sensing characteristics of the core/shell SiO$_2$/Au NCAs with different structural parameters as summarized in Fig. 6. We set the lattice constants of the NCAs as $a_\perp = 550$, 700, and 1000 nm for the NCs with diameters $D = 50$, 100, and 250 nm in order to tune the $(0, \pm1)$ superstrate diffraction orders to overlap with the resonance wavelength of the D$_2$ modes to achieve the plasmonic-photonic coupling. We choose the smaller $a_\parallel$ to tune the $(\pm1, 0)$ substrate diffraction orders to the shorter wavelength side of the LSPRs of the NCs to avoid the interference from the occurring of the parallel coupling. From Fig. 6, we can see that the coupling between the D$_1$ mode and $(0, \pm1)$ substrate diffraction orders disappears when the diameter of the NCs becomes small. Only small dips are observed in the spectra for $D = 50$ nm at RI = 1.2 and for $D = 100$ nm at RI = 1.16 and 1.2, indicating that the refractive-index mismatch between substrate and superstrate suppresses the LPMs when the polarizability of the NCs is not large enough (due to the small diameter of the NCs) to support the plasmonic-photonic coupling. In contrast, the height-induced LPM still exists even when the diameter of the NCs is reduced down to 50 nm. Therefore, different from the previously studied LPMs in the arrays of NPs with low aspect ratio where the plasmonic-photonic coupling and thus the LPMs are suppressed by the presence of substrates due to the asymmetric environments, [52, 62] the height-induced LPMs in the NCAs of high aspect ratio are robust under the asymmetric environments, which are frequently experienced in the on-chip sensing applications.

Figure 6d summarizes the FWHM and the coupling wavelength for the core/shell NCAs with the different structural parameters and superstrate RIs. The FWHM decreases when the RI increases due to the weakening coupling strength. By taking the FWHM for the NCAs with strong plasmonic-photonic coupling (i.e., RI = 1.12, 1.08, and 1.04 for $D = 50$, 100, and 250 nm), we calculate the FOM as 23.7, 22.4, and 13.2, respectively. The highest FOM obtained at $D = 50$ nm suggests that reducing the FWHM is critical in enhancing the FOM of the LPM-based plasmonic sensors. The high FOM for both large and small NCAs is also supported by theoretical analysis. According to Eq. 4, the wavelength sensitivity is determined by $a_\perp$, which decreases for the arrays with smaller NCs. However, the FWHM also decreases for the smaller NCs, which maintains the high FOM for the NCAs.

Summary

In summary, the substrate-independent LPMs, which arise from the coupling between superstrate diffraction orders and the height-induced modes of LSPRs in the lattice plasmon resonance structures of high aspect ratio (e.g., SiO$_2$/Au core/shell NCAs), presents a tremendous opportunity for the development of the high-performance, on-chip plasmonic sensors. The narrow linewidth and the high wavelength sensitivity of the substrate-independent LPMs lead to the sensors of high FOM for a wide range of working wavelengths. The high SNR of the plasmonic sensors is enabled by the LPM-associated large field enhancement in the NCAs. The proposed structures can be fabricated with low-cost and high-throughput nanofabrication techniques, including nanoimprinting lithography. With the high FOM, high SNR, and robustness of the substrate-independent LPMs, the on-chip plasmonic sensors will find a wide range of applications in molecular analysis, biomedicine, and environmental protection.

References

1. Halas NJ, Lal S, Chang WS, Link S, Nordlander P (2011) Plasmons in strongly coupled metallic nanostructures. Chem Rev 111(6): 3913–3961. doi:10.1021/cr200061k
2. Hao E, Schatz GC (2004) Electromagnetic fields around silver nanoparticles and dimers. J Chem Phys 120(1):357–366. doi:10.1063/1.1629280
3. Sherry LJ, Chang SH, Schatz GC, Van Duyne RP, Wiley BJ, Xia YN (2005) Localized surface plasmon resonance spectroscopy of single silver nanocubes. Nano Lett 5(10):2034–2038. doi:10.1021/nl0515753
4. Bukasov R, Ali TA, Nordlander P, Shumaker-Parry JS (2010) Probing the plasmonic near-field of gold nanocrescent antennas. ACS Nano 4(11):6639–6650. doi:10.1021/nn101994t
5. Klar T, Perner M, Grosse S, von Plessen G, Spirkl W, Feldmann J (1998) Surface-plasmon resonances in single metallic nanoparticles. Phys Rev Lett 80(19):4249–4252. doi:10.1103/PhysRevLett.80.4249
6. Lu D, Kan JJ, Fullerton EE, Liu Z (2014) Enhancing spontaneous emission rates of molecules using nanopatterned multilayer hyperbolic metamaterials. Nat Nanotechnol 9(1):48–53. doi:10.1038/nnano.2013.276
7. Gandra N, Portz C, Tian L, Tang R, Xu B, Achilefu S, Singamaneni S (2014) Probing distance-dependent plasmon-enhanced near-infrared fluorescence using polyelectrolyte multilayers as dielectric spacers. Angew Chem Int Ed 53(3):866–870. doi:10.1002/anie.201308516
8. Tanaka K, Plum E, Ou JY, Uchino T, Zheludev NI (2010) Multifold enhancement of quantum dot luminescence in plasmonic metamaterials. Phys Rev Lett 105(22):227403. doi:10.1103/PhysRevLett.105.227403
9. Dang X, Qi J, Klug MT, Chen P-Y, Yun DS, Fang NX, Hammond PT, Belcher AM (2013) Tunable localized surface plasmon-enabled

broadband light-harvesting enhancement for high-efficiency panchromatic dye-sensitized solar cells. Nano Lett 13(2):637–642. doi:10.1021/nl3043823

10. Mubeen S, Lee J, Lee W-r, Singh N, Stucky GD, Moskovits M (2014) On the plasmonic photovoltaic. ACS Nano 8(6):6066–6073. doi:10.1021/nn501379r

11. Neumann O, Feronti C, Neumann AD, Dong A, Schell K, Lu B, Kim E, Quinn M, Thompson S, Grady N, Nordlander P, Oden M, Halas NJ (2013) Compact solar autoclave based on steam generation using broadband light-harvesting nanoparticles. Proc Natl Acad Sci 110(29):11677–11681. doi:10.1073/pnas.1310131110

12. Mukherjee S, Zhou L, Goodman AM, Large N, Ayala-Orozco C, Zhang Y, Nordlander P, Halas NJ (2014) Hot-electron-induced dissociation of H2 on gold nanoparticles supported on SiO2. J Am Chem Soc 136(1):64–67. doi:10.1021/ja411017b

13. Atwater HA, Polman A (2010) Plasmonics for improved photovoltaic devices. Nat Mater 9(3):205–213. doi:10.1038/nmat2629

14. Pryce IM, Koleske DD, Fischer AJ, Atwater HA (2010) Plasmonic nanoparticle enhanced photocurrent in GaN/InGaN/GaN quantum well solar cells. Appl Phys Lett 96 (15). doi:10.1063/1.3377900

15. Roca M, Haes AJ (2008) Silica-void-gold nanoparticles: temporally stable surf ace-enhanced Raman scattering substrates. J Am Chem Soc 130(43):14273–14279. doi:10.1021/ja8059039

16. Jiao Y, Ryckman JD, Koktysh DS, Weiss SM (2013) Controlling surface enhanced Raman scattering using grating-type patterned nanoporous gold substrates. Opt Mater Express 3(8):1137–1148. doi:10.1364/ome.3.001137

17. Scarabelli L, Coronado-Puchau M, Giner-Casares JJ, Langer J, Liz-Marzán LM (2014) Monodisperse gold nanotriangles: size control, large-scale self-assembly, and performance in surface-enhanced Raman scattering. ACS Nano 8(6):5833–5842. doi:10.1021/nn500727w

18. Zheng YB, Payton JL, Song T-B, Pathem BK, Zhao Y, Ma H, Yang Y, Jensen L, Jen AKY, Weiss PS (2012) Surface-enhanced Raman spectroscopy to probe photoreaction pathways and kinetics of isolated reactants on surfaces: flat versus curved substrates. Nano Lett 12(10):5362–5368. doi:10.1021/nl302750d

19. Ayala-Orozco C, Urban C, Knight MW, Urban AS, Neumann O, Bishnoi SW, Mukherjee S, Goodman AM, Charron H, Mitchell T, Shea M, Roy R, Nanda S, Schiff R, Halas NJ, Joshi A (2014) Au nanomatryoshkas as efficient near-infrared photothermal transducers for cancer treatment: benchmarking against nanoshells. ACS Nano 8(6):6372–6381. doi:10.1021/nn501871d

20. Bardhan R, Lal S, Joshi A, Halas NJ (2011) Theranostic nanoshells: from probe design to imaging and treatment of cancer. Acc Chem Res 44(10):936–946. doi:10.1021/ar200023x

21. Willets KA, Van Duyne RP (2007) Localized surface plasmon resonance spectroscopy and sensing. Annu Rev Phys Chem 58:267–297. doi:10.1146/annurev.physchem.58.032806.104607

22. Anker JN, Hall WP, Lyandres O, Shah NC, Zhao J, Van Duyne RP (2008) Biosensing with plasmonic nanosensors. Nat Mater 7(6):442–453. doi:10.1038/nmat2162

23. Tian L, Liu K-K, Morrissey JJ, Gandra N, Kharasch ED, Singamaneni S (2014) Gold nanocages with built-in artificial antibodies for label-free plasmonic biosensing. J Mater Chem B 2(2):167–170. doi:10.1039/c3tb21551b

24. Zheng YB, Kiraly B, Weiss PS, Huang TJ (2012) Molecular plasmonics for biology and nanomedicine. Nanomedicine 7(5):751–770. doi:10.2217/nnm.12.30

25. Aćimović SS, Kreuzer MP, González MU, Quidant R (2009) Plasmon near-field coupling in metal dimers as a step toward single-molecule sensing. ACS Nano 3(5):1231–1237. doi:10.1021/nn900102j

26. Enoch S, Quidant R, Badenes G (2004) Optical sensing based on plasmon coupling in nanoparticle arrays. Opt Express 12(15):3422–3427. doi:10.1364/opex.12.003422

27. Mayer KM, Hafner JH (2011) Localized surface plasmon resonance sensors. Chem Rev 111(6):3828–3857. doi:10.1021/cr100313v

28. Mayer KM, Lee S, Liao H, Rostro BC, Fuentes A, Scully PT, Nehl CL, Hafner JH (2008) A label-free immunoassay based upon localized surface plasmon resonance of gold nanorods. ACS Nano 2(4):687–692. doi:10.1021/nn7003734

29. Chen C-D, Cheng S-F, Chau L-K, Wang CRC (2007) Sensing capability of the localized surface plasmon resonance of gold nanorods. Biosens Bioelectron 22(6):926–932. doi:10.1016/j.bios.2006.03.021

30. Mock JJ, Smith DR, Schultz S (2003) Local refractive index dependence of plasmon resonance spectra from individual nanoparticles. Nano Lett 3(4):485–491. doi:10.1021/nl0340475

31. Underwood S, Mulvaney P (1994) Effect of the solution refractive index on the color of gold colloids. Langmuir 10(10):3427–3430. doi:10.1021/la00022a011

32. Evans PR, Wurtz GA, Atkinson R, Hendren W, O'Connor D, Dickson W, Pollard RJ, Zayats AV (2007) Plasmonic core/shell nanorod arrays: subattoliter controlled geometry and tunable optical properties. J Phys Chem C 111(34):12522–12527. doi:10.1021/jp0718348

33. Cinel NA, Butun S, Ozbay E (2012) Electron beam lithography designed silver nano-disks used as label free nano-biosensors based on localized surface plasmon resonance. Opt Express 20(3):2587–2597. doi:10.1364/oe.20.002587

34. Vazquez-Mena O, Sannomiya T, Villanueva LG, Voros J, Brugger J (2011) Metallic nanodot arrays by stencil lithography for plasmonic biosensing applications. ACS Nano 5(2):844–853. doi:10.1021/nn1019253

35. Wokaun A, Gordon J, Liao P (1982) Radiation damping in surface-enhanced Raman scattering. Phys Rev Lett 48(14):957–960. doi:10.1103/PhysRevLett.48.957

36. Sonnichsen C, Franzl T, Wilk T, von Plessen G, Feldmann J, Wilson O, Mulvaney P (2002) Drastic reduction of plasmon damping in gold nanorods. Phys Rev Lett 88(7):077402. doi:10.1103/PhysRevLett.88.077402

37. Novo C, Gomez D, Perez-Juste J, Zhang Z, Petrova H, Reismann M, Mulvaney P, Hartland GV (2006) Contributions from radiation damping and surface scattering to the linewidth of the longitudinal plasmon band of gold nanorods: a single particle study. Phys Chem Chem Phys 8(30):3540–3546. doi:10.1039/b604856k

38. Kats MA, Yu N, Genevet P, Gaburro Z, Capasso F (2011) Effect of radiation damping on the spectral response of plasmonic components. Opt Express 19(22):21748–21753. doi:10.1364/oe.19.021748

39. Dmitriev A, Hägglund C, Chen S, Fredriksson H, Pakizeh T, Käll M, Sutherland DS (2008) Enhanced nanoplasmonic optical sensors with reduced substrate effect. Nano Lett 8(11):3893–3898. doi:10.1021/nl8023142

40. Nehl CL, Liao H, Hafner JH (2006) Optical properties of star-shaped gold nanoparticles. Nano Lett 6(4):683–688. doi:10.1021/nl052409y

41. Hao F, Sonnefraud Y, Dorpe PV, Maier SA, Halas NJ, Nordlander P (2008) Symmetry breaking in plasmonic nanocavities: subradiant LSPR sensing and a tunable Fano resonance. Nano Lett 8(11):3983–3988. doi:10.1021/nl802509r

42. Zhan Y, Lei DY, Li X, Maier SA (2014) Plasmonic Fano resonances in nanohole quadrumers for ultra-sensitive refractive index sensing. Nanoscale 6(9):4705–4715. doi:10.1039/c3nr06024a

43. Miroshnichenko AE, Flach S, Kivshar YS (2010) Fano resonances in nanoscale structures. Rev Mod Phys 82(3):2257–2298. doi:10.1103/RevModPhys.82.2257

44. Meier M, Wokaun A, Liao PF (1985) Enhanced fields on rough surfaces-dipolar interactions among particles of sizes exceeding the Rayleigh limit. J Opt Soc Am B: Opt Phys 2(6):931–949. doi:10.1364/JOSAB.2.000931

45. Markel VA (1993) Coupled-dipole approach to scattering of light from a one-dimensional periodic dipole structure. J Mod Opt 40(11):2281–2291. doi:10.1080/09500349314552291

46. Lamprecht B, Schider G, Lechner RT, Ditlbacher H, Krenn JR, Leitner A, Aussenegg FR (2000) Metal nanoparticle gratings: influence of dipolar particle interaction on the plasmon resonance. Phys Rev Lett 84(20):4721–4724. doi:10.1103/PhysRevLett.84.4721

47. Zhao LL, Kelly KL, Schatz GC (2003) The extinction spectra of silver nanoparticle arrays: influence of array structure on plasmon resonance wavelength and width. J Phys Chem B 107(30):7343–7350. doi:10.1021/jp034235j

48. Zou SL, Janel N, Schatz GC (2004) Silver nanoparticle array structures that produce remarkably narrow plasmon lineshapes. J Chem Phys 120(23):10871–10875. doi:10.1063/1.1760740

49. Zou SL, Schatz GC (2004) Narrow plasmonic/photonic extinction and scattering line shapes for one and two dimensional silver nanoparticle arrays. J Chem Phys 121(24):12606–12612. doi:10.1063/1.1826036

50. Auguie B, Barnes WL (2008) Collective resonances in gold nanoparticle arrays. Phys Rev Lett 101(14):143902. doi:10.1103/PhysRevLett.101.143902

51. Chu Y, Schonbrun E, Yang T, Crozier KB (2008) Experimental observation of narrow surface plasmon resonances in gold nanoparticle arrays. Appl Phys Lett 93(18):181108. doi:10.1063/1.3012365

52. Kravets VG, Schedin F, Grigorenko AN (2008) Extremely narrow plasmon resonances based on diffraction coupling of localized plasmons in arrays of metallic nanoparticles. Phys Rev Lett 101(8):087403. doi:10.1103/PhysRevLett.101.087403

53. Gao H, McMahon JM, Lee MH, Henzie J, Gray SK, Schatz GC, Odom TW (2009) Rayleigh anomaly-surface plasmon polariton resonances in palladium and gold subwavelength hole arrays. Opt Express 17(4):2334–2340. doi:10.1364/OE.17.002334

54. Zhou W, Odom TW (2011) Tunable subradiant lattice plasmons by out-of-plane dipolar interactions. Nat Nanotechnol 6(7):423–427. doi:10.1038/nnano.2011.72

55. Nikitin AG, Nguyen T, Dallaporta H (2013) Narrow plasmon resonances in diffractive arrays of gold nanoparticles in asymmetric environment: experimental studies. Appl Phys Lett 102(22):221116. doi:10.1063/1.4803535

56. Nikitin AG (2014) Diffraction-induced subradiant transverse-magnetic lattice plasmon modes in metal nanoparticle arrays. Appl Phys Lett 104(6):061107. doi:10.1063/1.4864277

57. Vitrey A, Aigouy L, Prieto P, García-Martín JM, González MU (2014) Parallel collective resonances in arrays of gold nanorods. Nano Lett 14(4):2079–2085. doi:10.1021/nl500238h

58. Spackova B, Homola J (2013) Sensing properties of lattice resonances of 2D metal nanoparticle arrays: an analytical model. Opt Express 21(22):27490–27502. doi:10.1364/oe.21.027490

59. Kuznetsov AI, Evlyukhin AB, Goncalves MR, Reinhardt C, Koroleva A, Arnedillo ML, Kiyan R, Marti O, Chichkov BN (2011) Laser fabrication of large-scale nanoparticle arrays for sensing applications. ACS Nano 5(6):4843–4849. doi:10.1021/nn2009112

60. Offermans P, Schaafsma MC, Rodriguez SRK, Zhang Y, Crego-Calama M, Brongersma SH, Rivas JG (2011) Universal scaling of the figure of merit of plasmonic sensors. ACS Nano 5(6):5151–5157. doi:10.1021/nn201227b

61. Du Y, Shi L, Hong M, Li H, Li D, Liu M (2013) A surface plasmon resonance biosensor based on gold nanoparticle array. Opt Commun 298:232–236. doi:10.1016/j.optcom.2013.02.024

62. Auguie B, Bendana XM, Barnes WL, Garcia de Abajo FJ (2010) Diffractive arrays of gold nanoparticles near an interface: critical role of the substrate. Phys Rev B 82(15):155447. doi:10.1103/PhysRevB.82.155447

63. Henzie J, Lee MH, Odom TW (2007) Multiscale patterning of plasmonic metamaterials. Nat Nanotechnol 2(9):549–554. doi:10.1038/nnano.2007.252

64. Shen Y, Zhou J, Liu T, Tao Y, Jiang R, Liu M, Xiao G, Zhu J, Zhou Z-K, Wang X, Jin C, Wang J (2013) Plasmonic gold mushroom arrays with refractive index sensing figures of merit approaching the theoretical limit. Nat Commun 4:2381. doi:10.1038/ncomms3381

65. Lin L, Yi Y (2014) Lattice plasmon resonance in core-shell SiO_2/Au nanocylinder arrays. Opt Lett 39(16):4823–4826. doi:10.1364/ol.39.004823

66. Lin L, Yi Y (2015) Orthogonal and parallel lattice plasmon resonance in core-shell SiO2/Au nanocylinder arrays. Opt Express 23(1):130–142. doi:10.1364/OE.23.000130

67. Westcott SL, Jackson JB, Radloff C, Halas NJ (2002) Relative contributions to the plasmon line shape of metal nanoshells. Phys Rev B 66(15):155431. doi:10.1103/PhysRevB.66.155431

68. Johnson P, Christy R (1972) Optical constants of the noble metals. Phys Rev B 6(12):4370–4379. doi:10.1103/PhysRevB.6.4370

69. Sönnichsen C, Geier S, Hecker NE, von Plessen G, Feldmann J, Ditlbacher H, Lamprecht B, Krenn JR, Aussenegg FR, Chan VZ-H, Spatz JP, Möller M (2000) Spectroscopy of single metallic nanoparticles using total internal reflection microscopy. Appl Phys Lett 77(19):2949–2951. doi:10.1063/1.1323553